

## Mapping the multiphase structure of H I in the Low-Latitude Intermediate-Velocity Arch 1

2 LUKA VUJEVA ,<sup>1,2,3,4</sup> ANTOINE MARCHAL ,<sup>5,2</sup> PETER G. MARTIN ,<sup>2</sup> AND MUKESH TAANK ,<sup>2,6</sup>

3 <sup>1</sup>*Department of Astronomy and Astrophysics, University of Toronto, 60 St. George Street, Toronto, ON M5S 3H8, Canada*

4 <sup>2</sup>*Canadian Institute for Theoretical Astrophysics, University of Toronto, 60 St. George Street, Toronto, ON M5S 3H8, Canada*

5 <sup>3</sup>*Cosmic Dawn Center (DAWN)*

6 <sup>4</sup>*Niels Bohr Institute, University of Copenhagen, Lyngbyvej 2, DK-2100 Copenhagen Ø*

7 <sup>5</sup>*Research School of Astronomy & Astrophysics, Australian National University, Canberra ACT 2610 Australia*

8 <sup>6</sup>*Department of Mathematics and Statistics, University of Guelph, 50 Stone Road E., Guelph, ON N1G 2W1, Canada*

9 (Received March 5, 2023; Revised --, --; Accepted --, --)

10 Submitted to ApJ

### ABSTRACT

11 We have analyzed the thermal and turbulent properties of the the Low-Latitude Intermediate-Velocity Arch 1.  
12 This was accomplished by using archival emission and absorption data from the GHIGLS 21 cm line survey at  
13 9.4' resolution, and the DHIGLS 21 cm line survey at 1' resolution. ROHSA was used to model the column density  
14 of different thermal phases, and to analyze absorption measurement. We find a spin temperature  $T_s \sim 75$  K, a  
15 cold gas mass fraction  $f \sim 0.5$ , and turbulent sonic Mach number  $M_t \sim 3.4$ , against the radio source 4C +66.09.  
16 The cold phase of LLIV1 appears as a collection of elongated filaments that forms a closed structure within the  
17 decomposed field. These sub-structures seem to follow the orientation of the overall large scale cloud, oriented  
18 along the diagonal of the GHIGLS field from north-west to south-east (in Galactic coordinates). The power  
19 spectrum of the cold phase is slightly shallower than that of the warm phase, quantifying that the cold phases  
20 have relatively more structure on small scales. Our spatially resolved map of the cold gas mass fraction in  
21 LLIV1 reveals important variation with  $0.1 \gtrsim f \gtrsim 0.9$ , with mean and standard deviation of 0.33 and 0.19,  
22 respectively. Our best model lacks the presence of unstable gas across the whole field of view, similar to the  
23 absorption line modeling against 4C +66.09. This possibly suggests that the transition is not on-going and has  
24 reached an equilibrium state.

25  
26 **Keywords:** Galaxy: halo – ISM: structure - kinematics and dynamics – Methods: observational - data analysis

### 1. INTRODUCTION

27 We have surveyed and analyzed the properties of H I  
28 line emission in an intermediate latitude field in Ursa Ma-  
29 jor ( $(\ell, b) = (143^\circ 6, 40^\circ 1)$  or  $(\alpha, \delta) = (09^\mathrm{h} 41^\mathrm{m}, 68^\circ 33')$ ),  
30 focusing on thermal condensation of warm neutral medium  
31 gas (WNM) to cold neutral medium gas (CNM) in the inter-  
32 mediate velocity component (IVC). This IVC gas is part of  
33 the Low-Latitude Intermediate-Velocity Arch (LLIV) (Kuntz  
34 & Danly 1996), in particular substructure LLIV1 (see their  
35 figure 2).

36 Maps of LLIV substructures in the velocity range  
37  $-60 \text{ km s}^{-1} < v < -30 \text{ km s}^{-1}$ , and  $-70 \text{ km s}^{-1} < v <$

38  $-30 \text{ km s}^{-1}$ , respectively, are shown in figures 12(b) and 16,  
39 respectively, of Wakker (2001). Their abundances measure-  
40 ments using lines of SII, NI, and OI indicate a metallicity  
41 that is approximately solar. Absorption of Fe and Si against  
42 PG 0804+762 ( $\ell, b) = (138^\circ 3, 31^\circ 0$ ) indicates some deple-  
43 tion onto dust grains (Richter et al. 2001). There is thermal  
44 dust emission morphologically correlated with the IVC gas  
45 in LLIV (Planck Collaboration XXIV 2011). Wakker (2001)  
46 constrain the distance to be in the range 0.9–1.8 kpc ( $z =$   
47 0.6–1.2 kpc). The implied mass is  $1.5 – 6 \times 10^5 M_\odot$ . Richter  
48 et al. (2003) report a relatively high detection rate of H<sub>2</sub> in  
49 the IVC gas, implying that CNM is ubiquitous, consistent  
50 with a key finding of our paper. Absorption lines toward  
51 PG 0804+762 (Richter et al. 2001) also indicate a substan-  
52 tial ionization fraction for hydrogen, about 20%. There is  
53 also hot coronal gas revealed by O VI absorption toward PG

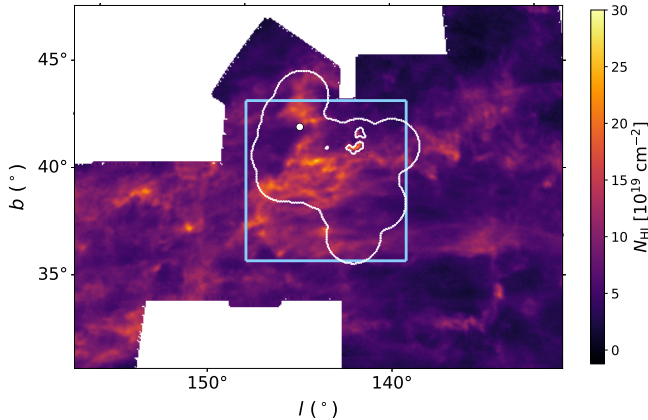


**Figure 1.** Integrated column density map of the GHIGLS NCPL mosaic in the IVC velocity range  $-81 \leq v \leq -27 \text{ km s}^{-1}$  showing the LLIV Arch. The light blue box shows the  $128 \times 128$  pixel region analyzed. The white contour outlines the DHIGLS UM field.

55 0804+762 (Richter et al. 2001) and C IV toward SN 1993J  
56 (de Boer et al. 1993).

57 Wakker (2001) notes how this is reminiscent of a Galactic  
58 fountain (Shapiro & Field 1976; Bregman 1980; Houck  
59 & Bregman 1990), where gas ejected into the Galactic Halo  
60 from inside the solar radius is expected to have a metallicity  
61 slightly above that in the local ISM, while the return flow is  
62 outside the Solar circle. Planck Collaboration XXIV (2011)  
63 show that dust appears to survive the hot phases of the flow  
64 (or to reform) and discuss the evolution of dust via shattering.  
65 What we find most interesting is that there is a substantial  
66 CNM apparently organized with the flow.

67 The paper is organized as follows. In Section 2 we present  
68 the H I data used in this work. Evidence for cold gas in  
69 LLIV1 based on H I absorption is summarized in Section 3.  
70 Section 4 describes the Gaussian decomposition performed  
71 to model the H I spectra, Sections 4.2 and 4.3 for GHIGLS  
72 and DHIGLS, respectively. (Appendices A and C present  
73 maps (2D spatial fields) characterizing each Gaussian com-  
74 ponent (column density, central velocity, velocity dispersion)  
75 for the respective data.) The identification of the different  
76 thermal phases is addressed, with attention to the robustness  
77 of the solution. Section 4.2.5 present a power spectrum anal-  
78 ysis of the phase maps, and Section 4.3.4 analyzes the cold  
79 gas mass fraction map inferred from the decomposed data.  
80 Finally, a summary is provided in Section 5.

## 81 2. H I DATA

### 82 2.1. GHIGLS (9'.4)

83 We used the GHIGLS<sup>1</sup> 21 cm line survey (Martin et al.  
84 2015) with spatial resolution of 9'.4 and velocity resolu-

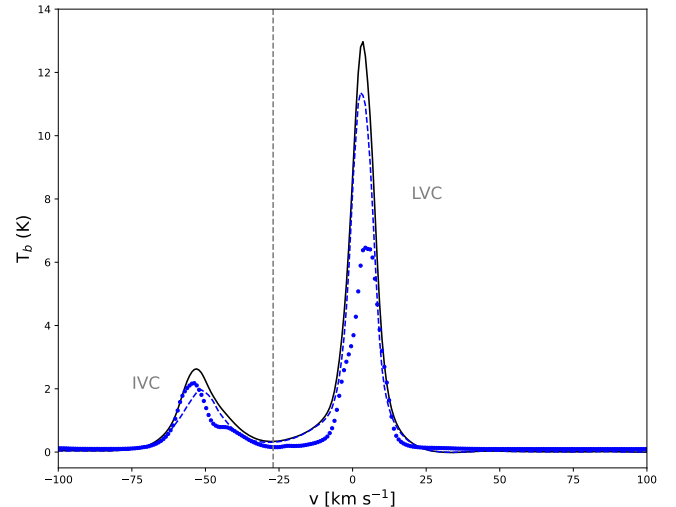


**Figure 2.** H I spectra characterizing the region analyzed in Ursa Major, the light blue box in Figure 1, showing the LLIV1 and the LVC gas. The black solid, blue dashed and blue dotted lines are the mean, median, and standard deviation spectra, respectively.

85 86 87 88 89 90 91 92 93 94 95 96 97 98 99 100 101 102 103 104 105 106 107 108 109 110 111 112 113 114 115 116 117 118 119 120 121 122 123 124 125 126 127 128 129 130 131 132 133 134 135 136 137 138 139 140 141 142 143 144 145 146 147 148 149 150 151 152 153 154 155 156 157 158 159 160 161 162 163 164 165 166 167 168 169 170 171 172 173 174 175 176 177 178 179 180 181 182 183 184 185 186 187 188 189 190 191 192 193 194 195 196 197 198 199 200 201 202 203 204 205 206 207 208 209 210 211 212 213 214 215 216 217 218 219 220 221 222 223 224 225 226 227 228 229 230 231 232 233 234 235 236 237 238 239 240 241 242 243 244 245 246 247 248 249 250 251 252 253 254 255 256 257 258 259 260 261 262 263 264 265 266 267 268 269 270 271 272 273 274 275 276 277 278 279 280 281 282 283 284 285 286 287 288 289 290 291 292 293 294 295 296 297 298 299 300 301 302 303 304 305 306 307 308 309 310 311 312 313 314 315 316 317 318 319 320 321 322 323 324 325 326 327 328 329 330 331 332 333 334 335 336 337 338 339 340 341 342 343 344 345 346 347 348 349 350 351 352 353 354 355 356 357 358 359 360 361 362 363 364 365 366 367 368 369 370 371 372 373 374 375 376 377 378 379 380 381 382 383 384 385 386 387 388 389 390 391 392 393 394 395 396 397 398 399 400 401 402 403 404 405 406 407 408 409 410 411 412 413 414 415 416 417 418 419 420 421 422 423 424 425 426 427 428 429 430 431 432 433 434 435 436 437 438 439 440 441 442 443 444 445 446 447 448 449 450 451 452 453 454 455 456 457 458 459 460 461 462 463 464 465 466 467 468 469 470 471 472 473 474 475 476 477 478 479 480 481 482 483 484 485 486 487 488 489 490 491 492 493 494 495 496 497 498 499 500 501 502 503 504 505 506 507 508 509 510 511 512 513 514 515 516 517 518 519 520 521 522 523 524 525 526 527 528 529 530 531 532 533 534 535 536 537 538 539 540 541 542 543 544 545 546 547 548 549 550 551 552 553 554 555 556 557 558 559 560 561 562 563 564 565 566 567 568 569 570 571 572 573 574 575 576 577 578 579 580 581 582 583 584 585 586 587 588 589 5810 5811 5812 5813 5814 5815 5816 5817 5818 5819 5820 5821 5822 5823 5824 5825 5826 5827 5828 5829 5830 5831 5832 5833 5834 5835 5836 5837 5838 5839 5840 5841 5842 5843 5844 5845 5846 5847 5848 5849 5850 5851 5852 5853 5854 5855 5856 5857 5858 5859 5860 5861 5862 5863 5864 5865 5866 5867 5868 5869 5870 5871 5872 5873 5874 5875 5876 5877 5878 5879 5880 5881 5882 5883 5884 5885 5886 5887 5888 5889 5890 5891 5892 5893 5894 5895 5896 5897 5898 5899 58100 58101 58102 58103 58104 58105 58106 58107 58108 58109 58110 58111 58112 58113 58114 58115 58116 58117 58118 58119 58120 58121 58122 58123 58124 58125 58126 58127 58128 58129 58130 58131 58132 58133 58134 58135 58136 58137 58138 58139 58140 58141 58142 58143 58144 58145 58146 58147 58148 58149 58150 58151 58152 58153 58154 58155 58156 58157 58158 58159 58160 58161 58162 58163 58164 58165 58166 58167 58168 58169 58170 58171 58172 58173 58174 58175 58176 58177 58178 58179 58180 58181 58182 58183 58184 58185 58186 58187 58188 58189 58190 58191 58192 58193 58194 58195 58196 58197 58198 58199 581910 581911 581912 581913 581914 581915 581916 581917 581918 581919 581920 581921 581922 581923 581924 581925 581926 581927 581928 581929 581930 581931 581932 581933 581934 581935 581936 581937 581938 581939 581940 581941 581942 581943 581944 581945 581946 581947 581948 581949 581950 581951 581952 581953 581954 581955 581956 581957 581958 581959 581960 581961 581962 581963 581964 581965 581966 581967 581968 581969 581970 581971 581972 581973 581974 581975 581976 581977 581978 581979 581980 581981 581982 581983 581984 581985 581986 581987 581988 581989 581990 581991 581992 581993 581994 581995 581996 581997 581998 581999 5819100 5819101 5819102 5819103 5819104 5819105 5819106 5819107 5819108 5819109 5819110 5819111 5819112 5819113 5819114 5819115 5819116 5819117 5819118 5819119 58191100 58191101 58191102 58191103 58191104 58191105 58191106 58191107 58191108 58191109 58191110 58191111 58191112 58191113 58191114 58191115 58191116 58191117 58191118 58191119 581911100 581911101 581911102 581911103 581911104 581911105 581911106 581911107 581911108 581911109 581911110 581911111 581911112 581911113 581911114 581911115 581911116 581911117 581911118 581911119 5819111100 5819111101 5819111102 5819111103 5819111104 5819111105 5819111106 5819111107 5819111108 5819111109 5819111110 5819111111 5819111112 5819111113 5819111114 5819111115 5819111116 5819111117 5819111118 5819111119 58191111100 58191111101 58191111102 58191111103 58191111104 58191111105 58191111106 58191111107 58191111108 58191111109 58191111110 58191111111 58191111112 58191111113 58191111114 58191111115 58191111116 58191111117 58191111118 58191111119 581911111100 581911111101 581911111102 581911111103 581911111104 581911111105 581911111106 581911111107 581911111108 581911111109 581911111110 581911111111 581911111112 581911111113 581911111114 581911111115 581911111116 581911111117 581911111118 581911111119 5819111111100 5819111111101 5819111111102 5819111111103 5819111111104 5819111111105 5819111111106 5819111111107 5819111111108 5819111111109 5819111111110 5819111111111 5819111111112 5819111111113 5819111111114 5819111111115 5819111111116 5819111111117 5819111111118 5819111111119 58191111111100 58191111111101 58191111111102 58191111111103 58191111111104 58191111111105 58191111111106 58191111111107 58191111111108 58191111111109 58191111111110 58191111111111 58191111111112 58191111111113 58191111111114 58191111111115 58191111111116 58191111111117 58191111111118 58191111111119 581911111111100 581911111111101 581911111111102 581911111111103 581911111111104 581911111111105 581911111111106 581911111111107 581911111111108 581911111111109 581911111111110 581911111111111 581911111111112 581911111111113 581911111111114 581911111111115 581911111111116 581911111111117 581911111111118 581911111111119 5819111111111100 5819111111111101 5819111111111102 5819111111111103 5819111111111104 5819111111111105 5819111111111106 5819111111111107 5819111111111108 5819111111111109 5819111111111110 5819111111111111 5819111111111112 5819111111111113 5819111111111114 5819111111111115 5819111111111116 5819111111111117 5819111111111118 5819111111111119 58191111111111100 58191111111111101 58191111111111102 58191111111111103 58191111111111104 58191111111111105 58191111111111106 58191111111111107 58191111111111108 58191111111111109 58191111111111110 58191111111111111 58191111111111112 58191111111111113 58191111111111114 58191111111111115 58191111111111116 58191111111111117 58191111111111118 58191111111111119 581911111111111100 581911111111111101 581911111111111102 581911111111111103 581911111111111104 581911111111111105 581911111111111106 581911111111111107 581911111111111108 581911111111111109 581911111111111110 581911111111111111 581911111111111112 581911111111111113 581911111111111114 581911111111111115 581911111111111116 581911111111111117 581911111111111118 581911111111111119 5819111111111111100 5819111111111111101 5819111111111111102 5819111111111111103 5819111111111111104 5819111111111111105 5819111111111111106 5819111111111111107 5819111111111111108 5819111111111111109 5819111111111111110 5819111111111111111 5819111111111111112 5819111111111111113 5819111111111111114 5819111111111111115 5819111111111111116 5819111111111111117 5819111111111111118 5819111111111111119 58191111111111111100 58191111111111111101 58191111111111111102 58191111111111111103 58191111111111111104 58191111111111111105 58191111111111111106 58191111111111111107 58191111111111111108 58191111111111111109 58191111111111111110 58191111111111111111 58191111111111111112 58191111111111111113 58191111111111111114 58191111111111111115 58191111111111111116 58191111111111111117 58191111111111111118 58191111111111111119 581911111111111111100 581911111111111111101 581911111111111111102 581911111111111111103 581911111111111111104 581911111111111111105 581911111111111111106 581911111111111111107 581911111111111111108 581911111111111111109 581911111111111111110 581911111111111111111 581911111111111111112 581911111111111111113 581911111111111111114 581911111111111111115 581911111111111111116 581911111111111111117 581911111111111111118 581911111111111111119 5819111111111111111100 5819111111111111111101 5819111111111111111102 5819111111111111111103 5819111111111111111104 5819111111111111111105 5819111111111111111106 5819111111111111111107 5819111111111111111108 5819111111111111111109 5819111111111111111110 5819111111111111111111 5819111111111111111112 5819111111111111111113 5819111111111111111114 5819111111111111111115 5819111111111111111116 5819111111111111111117 5819111111111111111118 5819111111111111111119 58191111111111111111100 58191111111111111111101 58191111111111111111102 58191111111111111111103 58191111111111111111104 58191111111111111111105 58191111111111111111106 58191111111111111111107 58191111111111111111108 58191111111111111111109 58191111111111111111110 58191111111111111111111 58191111111111111111112 58191111111111111111113 58191111111111111111114 58191111111111111111115 58191111111111111111116 58191111111111111111117 58191111111111111111118 58191111111111111111119 581911111111111111111100 581911111111111111111101 581911111111111111111102 581911111111111111111103 581911111111111111111104 581911111111111111111105 581911111111111111111106 581911111111111111111107 581911111111111111111108 581911111111111111111109 581911111111111111111110 581911111111111111111111 581911111111111111111112 581911111111111111111113 581911111111111111111114 581911111111111111111115 581911111111111111111116 581911111111111111111117 581911111111111111111118 581911111111111111111119 5819111111111111111111100 5819111111111111111111101 5819111111111111111111102 5819111111111111111111103 5819111111111111111111104 5819111111111111111111105 5819111111111111111111106 5819111111111111111111107 5819111111111111111111108 5819111111111111111111109 5819111111111111111111110 5819111111111111111111111 5819111111111111111111112 5819111111111111111111113 5819111111111111111111114 5819111111111111111111115 5819111111111111111111116

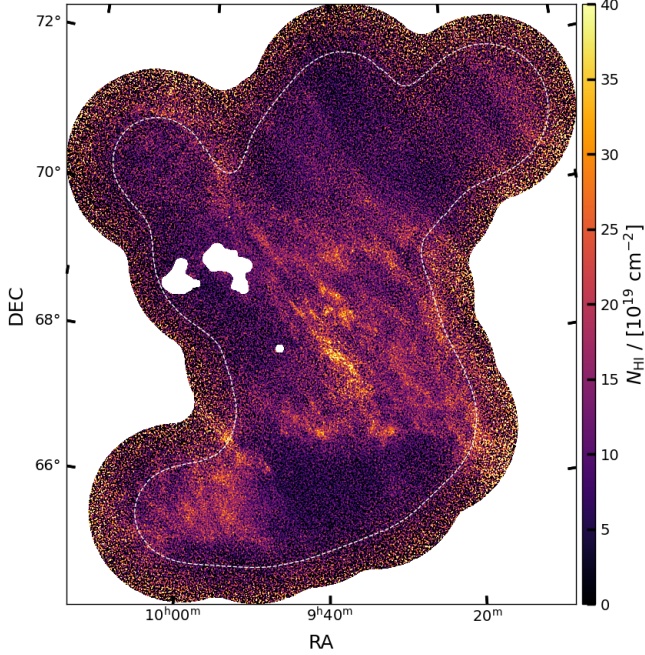


**Figure 3.** Integrated column density map of the IVC gas in UM from DHIGLS. The white dashed contours indicate where the noise has increased by a factor two relative to the minimum, and the white regions inside shows the masks applied to remove extra-galactic emission.

We also made use of the 58 square degree UM dataset, that was part of the DHIGLS<sup>2</sup> H I survey (Blagrave et al. 2017) with the Synthesis Telescope (ST) at the Dominion Radio Astrophysical Observatory. This field is located at  $(\alpha, \delta) = (09^{\text{h}}41^{\text{m}}, 68^{\circ}33')$  or  $(l, b) = (143.6, 40.1)$ . The UM field The 256-channel spectrometer, spacing  $\Delta v = 0.824 \text{ km s}^{-1}$  and velocity resolution  $1.32 \text{ km s}^{-1}$ , was centered at  $v_c = -60 \text{ km s}^{-1}$  relative to the Local Standard of Rest (LSR). The spatial resolution of the ST interferometric data was about  $1'$ . UM is embedded in the NPCL mosaic from GHIGLS shown in Figure 1. The DHIGLS UM product has the full range of spatial frequencies, obtained by a rigorous combination of the ST interferometric and GBT single dish data (see section 5 in Blagrave et al. 2017). The pixel size is  $18''$ .

Figure 3 presents the column density map of the IVC gas in UM (i.e., LLIV1), whose coverage is also annotated by the white line in Figure 1. Note the difference in coordinate systems; celestial coordinate for the DHIGLS data and Galactic coordinate for the GHIGLS data.

Unlike with the GBT, the high angular resolution of the ST (i.e.,  $1'$ ) allows the detection radio point sources with high continuum brightness temperatures. In their paper, Blagrave

et al. (2017) reported the detection of CNM gas with spin temperature  $T_s = 85 \text{ K}$  against the background radio galaxy 4C + 66.09 (NVSS<sup>3</sup> J094912 + 661459, Condon et al. 1998) with a continuum brightness temperature  $T_c = 444 \text{ K}$ , located within LLIV1 as annotated with white dots in Figures 1, 3, and 7 and dots in related figures. Following Taank et al. (2022), we used the original DHIGLS data to refine our spin temperature estimate by modeling the emission-absorption pair with Gaussians to allow for a better estimation of the cold component amplitude, and its turbulent properties.

### 3. EVIDENCE FOR COLD GAS FROM H I ABSORPTION IN LLIV1

We find that the absorption spectrum is well described by a single Gaussian component together with a quadratic polynomial to describe the local the baseline Parameters  $\mu_n$ ,  $\sigma_n$ , and  $T_n$  of the Gaussian are tabulated in Table 1.

The associated emission line was obtained by averaging data in an annulus centered on the source with an inner radius  $r_{\text{in}} = 1.2'$  and an outer radius  $r_{\text{out}} = 3'$  (i.e., 4 and 10 pixels of size  $18''$ , respectively). The resulting spectrum is well fit by a sum of two Gaussians, a narrow and a broad component. The CNM mass fraction is  $f_{\text{CNM}} = 0.51$ . Parameters  $\mu_b$ ,  $\sigma_b$ , and  $T_b$  of the narrow Gaussian are tabulated in Table 1 (method 1). Following Blagrave et al. (2017), the numbers from Table 1 lead to a spin temperature of  $T_s = 76.3 \text{ K}$ , slightly lower than their estimate without profile fitting.

Alternatively (method 2), we performed a Gaussian fit of a  $64 \times 64$  pixel grid centered on the source with ROHSA. Two Gaussians are needed to fully encode the signal as well. Parameters  $\mu_b$ ,  $\sigma_b$ , and  $T_b$  of the narrowest Gaussian at the position of the source are interpolated from the ROHSA parameter maps in the same annulus and are also tabulated in Table 1. The spin temperature evaluates to  $T_s = 72.2$ , and we find  $f_{\text{CNM}} = 0.55$ .

Following the procedure described in Taank et al. (2022, see their section 5.1.2), we separated the thermal and non-thermal broadening,  $\sigma_{\text{th}}$  and  $\sigma_{\text{nt}}$ , respectively, of the line and calculated the associated turbulent Mach number  $M_t$ . These are also tabulated in Table 1 for method 1 and method 2.

## 4. SPECTRAL DECOMPOSITION

### 4.1. ROHSA

ROHSA is a regularized optimization algorithm that decomposes PPV emission cubes into a sum of Gaussians (Marchal et al. 2019). ROHSA takes into account the spatial coherence of the emission and its multi-phase nature to perform a separation of different thermal phases. The methodology used in this work is similar to the one used in Taank et al. (2022). No-

<sup>2</sup> DRAO H I Intermediate Galactic Latitude Survey: <https://www.cita.utoronto.ca/DHIGLS/>

<sup>3</sup> NRAO VLA Sky Survey: <https://www.cv.nrao.edu/nvss/>

**Table 1.** Parameters<sup>a</sup> of the absorption feature in LLIV1 against 4C +66.09, interpolated emission, and derived  $T_s$  from DHIGLS data

Method	$T_c$	$\mu_n$	$\sigma_n$	$T_n$	$\mu_b$	$\sigma_b$	$T_b$	$T_s$	$\sigma_{\text{th}}$	$\sigma_{\text{nt}}$	$f_{\text{CNM}}$	$M_t$
1	444	2.43	1.52	-109	2.67	1.77	22.41	76.3	0.80	1.31	0.51	3.3
2	444	2.43	1.52	-109	2.66	1.99	22.73	72.2	0.80	1.30	0.55	3.4

<sup>a</sup> Velocities in  $\text{km s}^{-1}$  and temperatures in K.

184 **tably, we refer the reader to their section 3 for a comprehensive**  
 185 **description of ROHSA and its user-parameters, including**  
 186 **the number of Gaussians  $N$  and the set of hyper-parameters**  
 187 **( $\lambda_a, \lambda_\mu, \lambda_\sigma, \lambda''_\sigma$ ), as well as a noise prescription of the data. A**  
 188 **ROHSA decomposition requires the user to choose this set of**  
 189 **parameters to obtain a practicable solution and this must be**  
 190 **revisited for a given data set (e.g., Marchal et al. 2021; Taank**  
 191 **et al. 2022).**

192 **For GHIGLS data, we described the noise properties by**  
 193 **adopting the 3D prescription discussed by Boothroyd et al.**  
 194 **(2011),  $S(v, \mathbf{r}) = S_e(\mathbf{r})(1 + T_b(\mathbf{r})/T_{\text{sys}})$ , where the 2D map of**  
 195 **the standard deviation of the noise  $S_e(\mathbf{r})$  is calculated from**  
 196 **emission-free end channels (in the case of GHIGLS, supplied**  
 197 **with the archival data), and  $T_{\text{sys}}$  is the system temperature,**  
 198 **typically 20 K for the GBT L-band observations. We used**  
 199 **the augmented version of the ROHSA code employed by Taank**  
 200 **et al. (2022) to work with 3D noise, rather than the standard**  
 201 **2D noise. For the DHIGLS data, we used the original imple-**  
 202 **mentation of ROHSA that considers  $S_e(\mathbf{r})$ .**

## 4.2. GHIGLS

### 4.2.1. User parameters

The solution presented in this work was obtained using the set parameters ( $N = 6, \lambda_a = \lambda_\mu = \lambda_\sigma = 40, \lambda''_\sigma = 50$ ). The number of Gaussians  $N$  required to fit the data was found to obtain a solution that fully describes the signal in the IVC range (i.e., LLIV1) without over-fitting the data. This was accomplished by decomposing the data with varying  $N$  in the range  $N = [5 - 9]$  and we used the per-channel mean contribution to chi-square,

$$\langle \chi^2 \rangle = \sum_r \left( \frac{L(v, \theta(\mathbf{r}))}{S(v, \mathbf{r})} \right)^2 / 128^2, \quad (1)$$

205 **to determine the goodness of fit.  $L(v, \theta(\mathbf{r}))$  is the residual**  
 206 **between the Gaussian model and the data.  $\theta_n(\mathbf{r}) =$**   
 207 **( $\mathbf{a}_n(\mathbf{r}), \mu_n(\mathbf{r}), \sigma_n(\mathbf{r})$ ): amplitude  $\mathbf{a}_n \geq \mathbf{0}$ , mean velocity  $\mu_n$ ,**  
 208 **and standard deviation  $\sigma_n$  parameterizes the  $N$  Gaussians of**  
 209 **the model prescribed in ROHSA. Note that  $128^2$  is the total**  
 210 **number of pixels inside the white box shown in Figure 1.**

211 **Figure 4 shows the mean contribution to chi-square  $\langle \chi^2 \rangle$**   
 212 **for varying  $N$ .  $N = 6$  provides a solution where  $\langle \chi^2 \rangle$  is higher**  
 213 **than unity denoted by the horizontal dashed line. For  $N > 6$ ,**

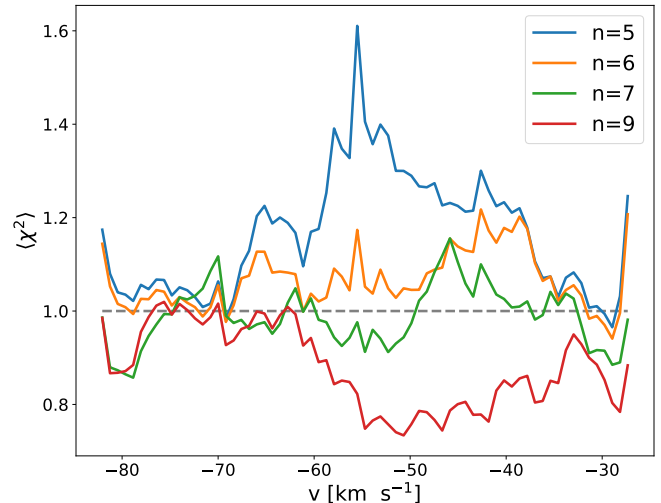


**Figure 4.** Spectrum of mean contribution to chi-square for Gaussian models fit with different number of Gaussians. Horizontal line indicates  $\langle \chi^2 \rangle = 1$ .

214  **$\langle \chi^2 \rangle$  is dominated by values lower than unity which indicate**  
 215 **an over-fit of the data. Figure 5 shows a reduced and spatially**  
 216 **resolved version of Equation 1,**

$$\chi^2_r(\theta(\mathbf{r})) = \sum_v \left( \frac{L(v, \theta(\mathbf{r}))}{S(v, \mathbf{r})} \right)^2 / k, \quad (2)$$

217 **where  $k = 69 - 3N$  is the number of degrees of freedom,**  
 218 **with 69 the number of velocity channels. Note that spectra**  
 219 **that were in-painted prior to decomposing the data were not**  
 220 **considered and are shown with masked regions. Our best**  
 221 **model achieves a mean chi-squared value across the field of**  
 222 **1.4, with median and standard deviation of 1.3 and 0.4, re-**  
 223 **spectively.**

224 **The hyper-parameters which control the smoothness of the**  
 225 **Gaussian parameter maps were chosen to be the same due**  
 226 **to their similar functional form, and to limit the parameter**  
 227 **space explored to find a practicable solution. They were cho-**  
 228 **sen empirically to correlate adjacent pixels on a spatial scale**  
 229 **close to the beam of the instrument. In experimenting with**  
 230 **this set of parameters, the optimal model was found to have**  
 231  **$\lambda_a = \lambda_\mu = \lambda_\sigma = 40$ .**

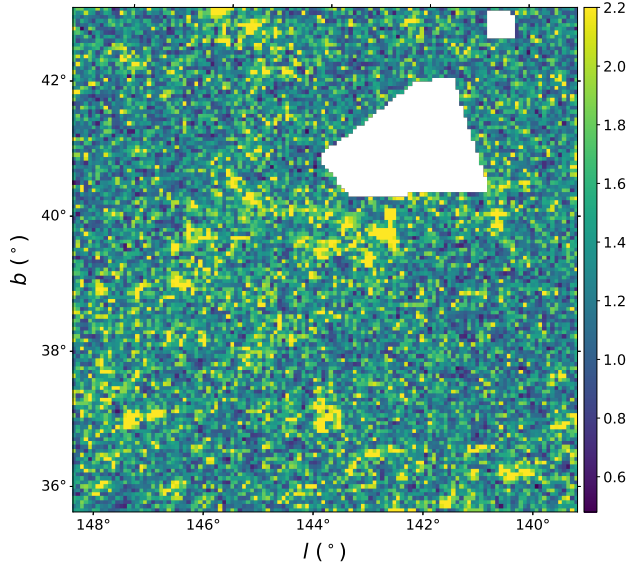


**Figure 5.** Map of the reduced  $\chi^2_r$  obtained with ROHSA on the GHIGLS data of LLIV1. Masked regions corresponds to pixels contaminated by extra-galactic emission and in-painted before decomposition.

**Table 2.** Mean kinematic properties (in  $\text{km s}^{-1}$ ) of Gaussians encoding the IVC gas (LLIV1) in the GHIGLS and DHIGLS data

Survey	$G_0$	$G_1$	$G_2$	$G_3$	$G_4$	$G_5$
GHIGLS	$\langle \mu_n \rangle$	-73.6	-58.7	-55.6	-52.9	-48.7
	$\langle \sigma_n \rangle$	6.8	5.7	2.1	2.0	5.8
DHIGLS	$\langle \mu_n \rangle$		-58.2	-55.2	-50.5	-45.7
	$\langle \sigma_n \rangle$		6.6	2.3	2.1	5.2
						10.0

To ensure a solution in which phases are identifiable according to distinct velocity dispersions (phase separation), we did a exploration the  $\lambda''_\sigma$  parameter, which controls the variance of the velocity dispersion of Gaussian component. We experimented  $\lambda''_\sigma = 1, 10, 20, 50, 100, 500, 1000$ , and found that 50 allows a coherent phase separation (see Section 4.2.2), without adding to much penalty on the global cost function prescribed in ROHSA that would prevent a overall good fit of the data.

#### 4.2.2. A representative solution

The corresponding Gaussian parameters for all spatial pixels are summarized in the two dimensional histogram of the column density-weighted  $\sigma - \mu$  parameters, seen in Figure 6. There are six clusters of points that correspond to the  $N$  Gaussians used by ROHSA to fit the data. Black points show the

column density-weighted average of each cluster which are summarized in Table 2. The velocity dispersions of all clusters range from about one to nine  $\text{km s}^{-1}$ . This reveals the multiphase nature of the gas in LLIV1.

We observe a clear separation of clusters along the dispersion velocity axis, denoted by the grey horizontal dashed line.  $G_0, G_1, G_4$  and  $G_5$  are broad, typical of warm gas, while  $G_2$  and  $G_3$  are narrow and can be associated to the cold phase of LLIV1. Interestingly, unlike what was found in the North Ecliptic Pole field from GHIGLS (Marchal et al. 2019; Marchal & Miville-Deschénes 2021), the NCPL (Taank et al. 2022), and the HVC complex C (Marchal et al. 2021), there is no Gaussian component with intermediate width characteristic of the presence of lukewarm gas associated with the unstable medium. This possibly suggests that the transition is not on-going has reached an equilibrium state. Along the velocity axis, the components  $G_1$  to  $G_4$  are located near the peak of LLIV1 as shown in Figure 2.  $G_0$  describes gas in the HVC range that is not of interest in this work and  $G_5$  gas located in the bridge between the LVC and emission from LLIV1.

The corresponding Gaussian parameter maps, sorted by increasing mean velocity, are presented in Appendix A. Column density maps, velocity maps, and dispersion velocity maps of the 6 Gaussian components are shown in Figures A1, A2 and A3, respectively. By visualizing each column density map, we found that  $G_1, G_2, G_3$ , and  $G_4$  show a morphological correlation, not shared with  $G_0$  and  $G_5$ . In the following sections, only the four Gaussian components within the two vertical dashed line were kept.

#### 4.2.3. Uncertainties

To explore the degeneracy of the solution, we generated a model cube from the representative solution shown in Figure 6, and we repeated the Gaussian decomposition using three series of runs (Marchal et al. 2021; Taank et al. 2022). The first series explores how the outcome of the decomposition is influenced by the injection of 50 different instance of the noise. The hyper-parameters were kept the same. The second series explores the impact of the hyper-parameters on the solution. It entails generating 50 runs using random perturbations of the four ROHSA hyper-parameters in a  $\pm 10\%$  interval around the original values. Here, the injected 3D Gaussian random was kept the same. The third explores the sensitivity to how ROHSA is initialized by generating 50 runs where the four Gaussians needed to initialize ROHSA are randomly selected from the original  $\sigma - \mu$  diagram shown in Figure 6. We refer the reader to Taank et al. (2022) for further details of the procedure.

For each of the 50-run series, the outcomes were examined in  $\sigma - \mu$  space, showing that the clusters observed in Figure 6 are quite stable, including the lack of components with inter-

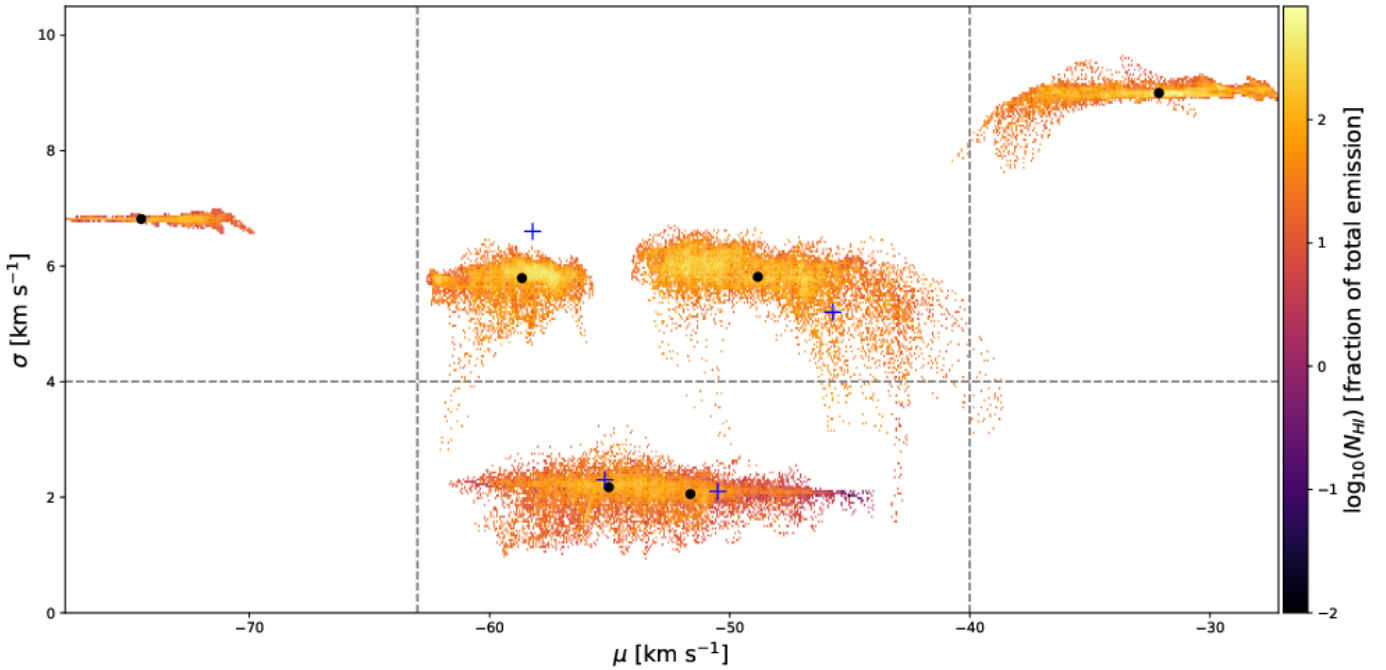


**Figure 6.** Two-dimensional probability distribution function of  $\sigma$  and  $\mu$  of the six Gaussians, weighted by their column densities obtained by decomposing the GHIGLS data of LLIV1 with ROHSA. The black dots correspond to the column density means of each cluster. The blue crosses show the same quantity but for the decomposition of the DHIGLS data within the selected velocity range. The horizontal dotted grey line shows the separation between the identified two thermal phases. The vertical grey lines show the velocity range where Gaussian components encodes emission from LLIV1.

mediate velocity dispersions. For each run, we performed a phase separation by grouping the four Gaussians into two categories based on their mean velocity dispersion; Gaussians with  $\langle \sigma_n \rangle > 4 \text{ km s}^{-1}$  were classified as WNM and Gaussians with  $\langle \sigma_n \rangle < 4 \text{ km s}^{-1}$  were classified as CNM. For each series, maps of the mean column density and its standard deviation were generated for the two components. All 50 runs of each series were combined to calculate maps of column density and corresponding standard deviations. Finally, the contributions from the three series were summed in quadrature to yield the total uncertainty.

#### 4.2.4. Phase maps

Figure 7 shows the column density maps (first column) with their associated uncertainty maps (second column) of the cold (top) and warm phases (bottom) in the GHIGLS data of LLIV1. Although we note some variations of the uncertainties across the field, their low values relative to the associated column densities reflects the high stability of the solution found with ROHSA.

The cold phase of LLIV1 appears as a collection of elongated filaments that forms a closed structure within the decomposed field. These sub-structures seem to follow the orientation of the overall large scale cloud, oriented along the diagonal of the field from north-west to south-east. Furthermore, they reassembles structures seen in the total column density map shown in Figure 1 which indicates that the frac-

tion of cold gas in LLIV1 is relatively high. This will be quantified in the following Section 4.3.4. The column density of the more diffuse warm phase is the highest within the contour delimited by the presence of cold gas, but also exists outside of LLIV1.

#### 4.2.5. Power spectrum

We statistically quantified and compared the multi-scale structure of the two phases by calculating their power spectrum  $P(k)$ , the azimuthal average of the modulus of the Fourier transform of their column density field. We modelled them as  $P(k) = B(k) \times P_0 k^\gamma + A \times N(k)$ , where  $P_0$  is the amplitude of the power spectrum,  $\gamma$  is the scaling exponent,  $B(k)$  describes the cutoff of the spectrum at high  $k$  due to the beam of the instrument, assumed to be a 2D Gaussian of FWHM = 9.4', and  $N(k)$  is the noise estimated by taking the power spectrum of empty channel maps of the PPV cube and scaled by a multiplicative factor  $A$ . The finite images were apodized using a cosine function to minimize systematic edge effects from the implementation of the Fourier transform.

Figure 8 show  $P(k)$  for the cold and warm phases, in blue and red dots respectively. The total fitted model is shown by the dashed dark blue and red lines for the cold and warm phases respectively. Recognizing the uncertainties, we find that the scaling exponent for the cold phase  $\gamma_{\text{CNM}} = -2.230 \pm 0.002$  is higher than that of the warm phase with  $\gamma_{\text{WNM}} = -2.613 \pm 0.003$ . In other words, the power spec-

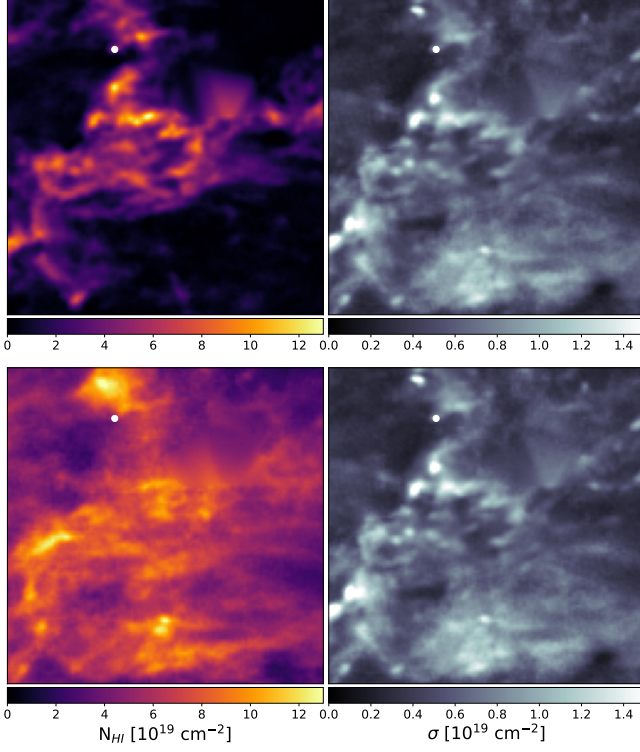


**Figure 7.** Column density maps (first column) with their associated uncertainties (second column) of the cold (top) and warm (bottom) phases in the GHIGLS data of LLIV1. The white dot denotes the position of the absorption feature against 4C +66.09.

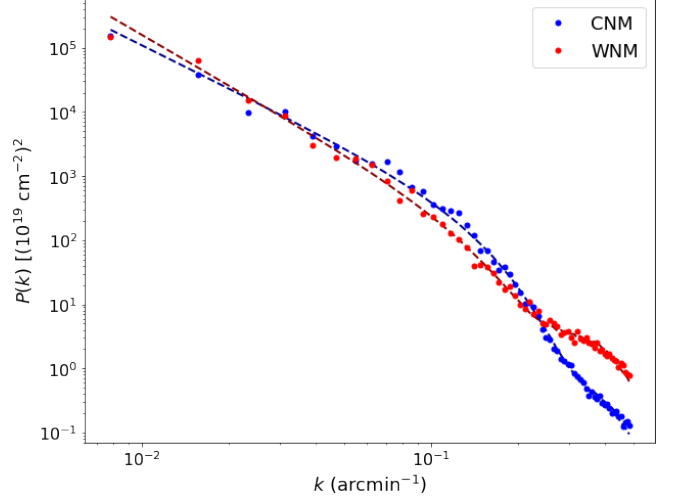


**Figure 8.** Power spectrum  $P(k)$  of the integrated column density of the cold (blue) and warm (red) phases. The dashed lines represent the models fit to each phase independently.

973 9'4 with a green line and blue line, respectively. The model  
974 fit to the DHIGLS data is shown by the red line.

975 To obtain a consistent solution at various resolution (from  
976 the native 1' beam to the 9'4 beam of the GHIGLS data), we  
977 used the value tabulated in Table 2 as initial parameters to  
978 start the multi-resolution prescribed in ROHSA (Marchal et al.  
979 2019; Taank et al. 2022). Only the five components whose  
980 mean velocities were included in the velocity range covered  
981 by the DHIGLS data where used; Gaussians  $G_1$  to  $G_5$ .

550 trum of the cold phase in slightly shallower than that of the  
551 warm phase, quantifying that the cold phases have relatively  
552 more structure on small scales. This is similar to what was  
553 found by Marchal & Miville-Deschénes (2021) and Marchal  
554 et al. (2021) in high latitude solar neighborhood gas of the  
555 NEP field of the GHIGLS survey, and the HVC complex C  
556 analyzed with DHIGLS data (the EN field).

### 4.3. DHIGLS

#### 4.3.1. Initialization

599 We performed a first exploration of the user-parameters us-  
600 ing the same methodology as described in Section 4.2.1. This  
601 search resulted in a set of parameters ( $N = 5$ ,  $\lambda_a = \lambda_\mu =$   
602  $\lambda_\sigma = 10$ ,  $\lambda''_\sigma = 10$ ) that could satisfy our selection criteria,  
603 including the flat  $\chi^2_r$  map with a mean value close to unity.  
604 This solution although statistically good was found to be im-  
605 practicable. After generated the model cube and applying  
606 a convolution to both the model and the data to lower their  
607 spatial resolution, the model was no longer providing a good  
608 description of the data. Specifically, the solution was found  
609 to have only one narrow Gaussian to describe the cold gas  
610 while the convolved data show two distinct peaks at a reso-  
611 lution as low as 2'. Figure B4 illustrates this by showing the  
612 original data (black line), and the convolved data at 2' and

#### 4.3.2. Solution and Uncertainties

628 An appropriate set of hyper-parameters was found to be  
629  $(\lambda_a = \lambda_\mu = \lambda_\sigma = 10, \lambda''_\sigma = 10)$ . The resulting decomposition  
630 still satisfies all our selection criteria, with a fairly uniform  $\chi^2_r$   
631 map (not shown here), showing no evidence of an overfitting  
632 of the data.

633 The mean kinematic properties of the five Gaussians used  
634 to describe the DHIGLS data are tabulated in Table 2; labeled  
635 from  $G_1$  to  $G_6$ . Values of the components  $G_1$  to  $G_4$  (associ-  
636 ated to LLIV1) are also denoted by blue crosses in Figure 6,  
637 and appear to be fairly consistent with those obtained from  
638 the decomposition of the GHIGLS data.

639 The corresponding Gaussian parameter maps, sorted by in-  
640 creasing mean velocity, are presented in Appendix C. Col-  
641 umn density maps, velocity maps, and dispersion velocity  
642 maps of the five Gaussian components are shown in Fig-  
643 ure C5. Visualization of each column density map shows  
644 similar morphology (and morphological correlation between  
645 components) than that of the GHIGLS solution, described  
646 in Section 4.2.2. Building on this solution, we followed the  
647 same methodology as described in Section 4.2.3 to eval-  
648 uate the mean column density and uncertainty maps for each

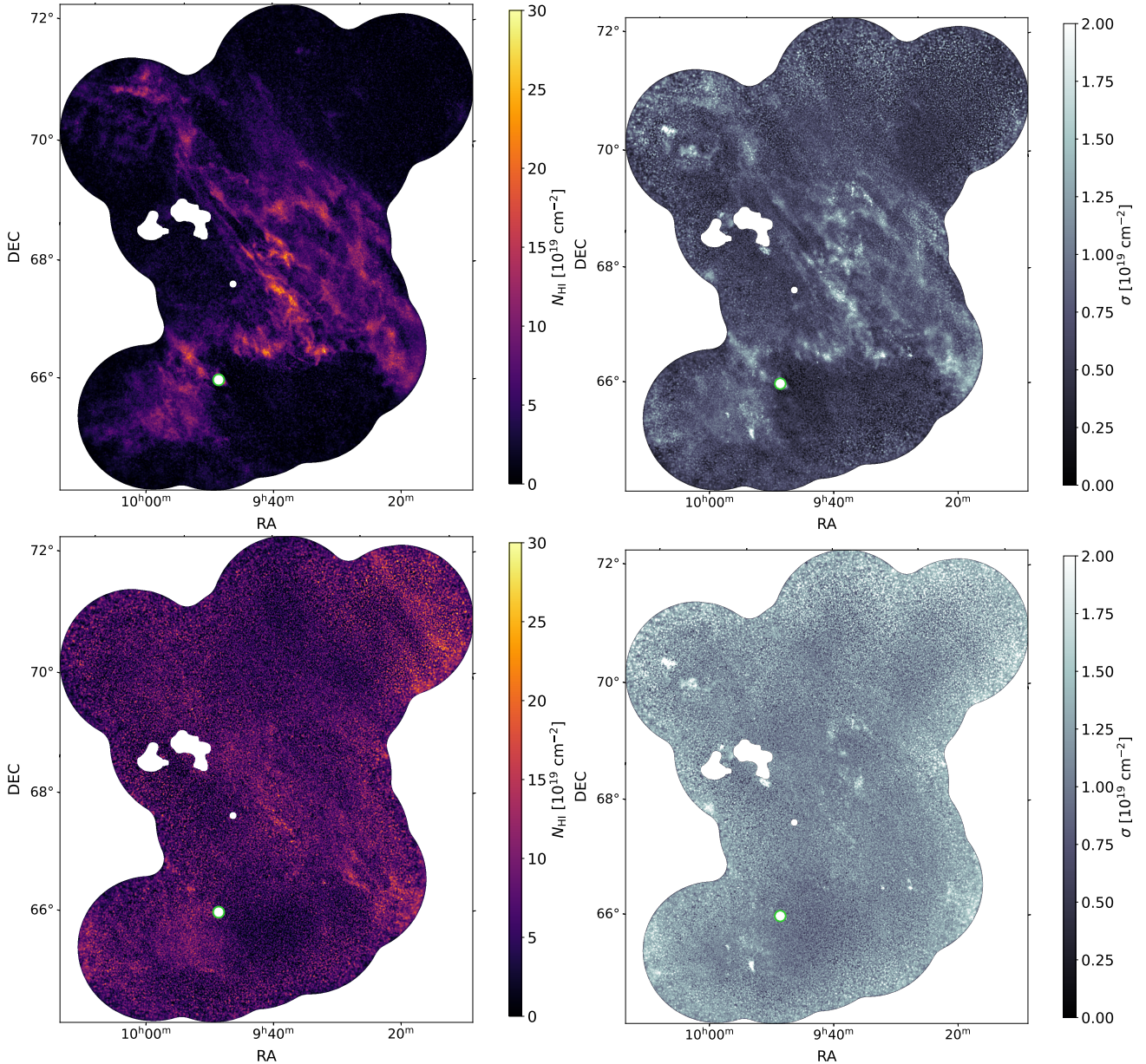


**Figure 9.** Column density maps (first column) with their associated standard deviation maps (second column) of the cold (top) and warm (bottom) phases in the DHIGLS data of LLIV1. The white dot with the green outline denotes the position of the absorption feature against 4C +66.09

404 phase. The top and bottom panels in Figure 9 show the re-  
405 sulting maps for the cold and warm phases, respectively.

#### 406 4.3.3. Comparison with GHIGLS

407 Our modeling of the cold phase in LLIV1 at high resolu-  
408 tion ( $1'$ ) reveals similar large scale properties than the  $9.4'$   
409 modeling obtained with GHIGLS data; the cold phase seems  
410 to be confined within a close contour, surrounded or mixed  
411 with its warm counterpart. The global orientation of LLIV1  
412 and the filamentary structure within suggests that there is a

413 bulk motion of the gas cloud on the plane of the sky (from  
414 top left to bottom right in Celestial coordinate).

415 The cold filamentary structures appears thinner at this res-  
416 olution, and the typical width of some filaments likely reach  
417 the size of the  $1'$  beam of the ST. This is notably the case of  
418 the highly elongated filament seen at the edge of the cloud  
419 located on the right hand side of the masked regions within  
420 the field, and oriented along its diagonal (from top left to  
421 bottom right). Clustering those filaments and analyzing their  
422 statistical properties is beyond the scope of this paper but will

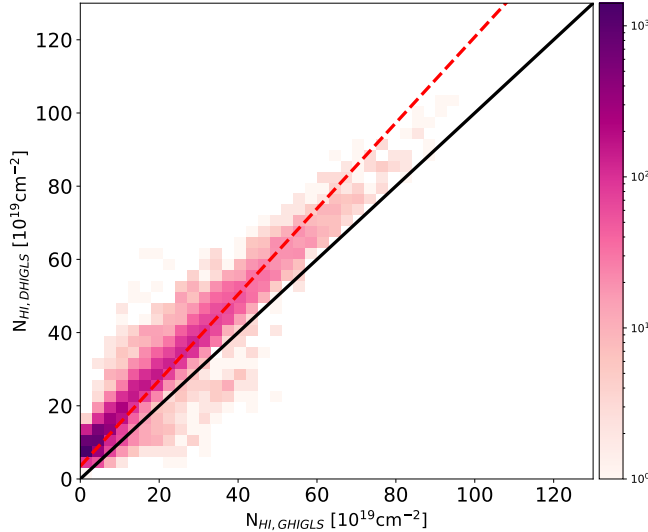


**Figure 10.** 2D histogram of the column density maps of the cold phase of the DHIGLS model vs the GHIGLS model. The 1:1 line is denoted by the solid black line and the dashed red line shows the linear fit using the bisector estimate.

provide in the further work valuable insight about the thermal condensation that has occurred (or is occurring) in LLIV1.

Finally, we compared the column density maps of the cold phase obtained from the two surveys in a 2D histogram shown in Figure 10. This was obtained by convolving the DHIGLS model at the 9.4 resolution of the GBT and by re-projecting it on the grid of the GHIGLS data. We observe a good correlation between the two though with a slope steeper than the 1:1 line annotated by the solid black line. A linear fit using the bisector estimator yielded a slope and intercept of  $1.17 \pm 6.92 \times 10^{-5}$  and  $3.50 \pm 2.07 \times 10^{-3}$ , respectively. This linear fit is shown by the red dashed line. A possible explanation is the difference in coverage between the two fields (Fig. 1, resulting in gaussians being used to model nearby gas that may not lie in one field or another. Although the comparison was made after masking both regions to fit within the DHIGLS UM field, the gaussians that were used for the GHIGLS decompositions are still responsible for modelling the gas outside of this mask, thus potentially creating variance between the decompositions of the two fields.

#### 4.3.4. CNM mass fraction

The left panel in Figure 11 shows our best model of the cold gas mass fraction  $f(\mathbf{r})$  in LLIV1 at the 1' resolution of the ST, and the left panel shows the corresponding uncertainties.  $f(\mathbf{r})$  shows large variations across the field ( $0.1 \gtrsim f \gtrsim 0.9$ ), and even within the contour delimiting the large scale extent of the cold phase. The mean and standard deviation of  $f(\mathbf{r})$  are 0.33 and 0.19, respectively.  $f(\mathbf{r})$  interpolated at the position of the absorption measurement (against 4C +66.09) is  $0.46 \pm 0.06$ , close to the values tabulated in Table 1.

The spatial distribution (i.e., morphological structure) of  $f(\mathbf{r})$  reassemble the column density map of the cold phase only, due to a relatively constant (i.e., flat) column density observed in the warm phase within the sky coverage of the DHIGLS data. Specifically,  $f(\mathbf{r})$  shows the same elongated filaments, as well as finger-like structures which seem to be part of an organized series of scalloping structures at the edge of LLIV1 oriented perpendicularly to the main orientation of the cloud and large filaments. This is particularly reminiscent of the structure observed in the Draco Nebula (Miville-Deschénes et al. 2017, and reference within), an other IVC that is though to be part of the Galactic fountain process of the Galaxy.

## 5. SUMMARY

Our novel study of the multi-phase properties of LLIV1 is based on H I spectra from GHIGLS and DHIGLS. We used ROHSA to decompose the spectral data in emission to model their multiphase structure and corroborated this with an absorption spectrum that were available. The main conclusions are as follows.

- From absorption line measurement in LLIV1 against 4C +66.09, we find a spin temperature  $T_s \sim 75$  K, a cold gas mass fraction  $f \sim 0.5$  (with no component associated to the unstable medium), and turbulent sonic Mach number  $M_t \sim 3.4$ , characteristic of supersonic turbulence in the cold phase.
- The cold phase of LLIV1 appears as a collection of elongated filaments that forms a closed structure within the decomposed field. These sub-structures seem to follow the orientation of the overall large scale cloud, oriented along the diagonal of the GHIGLS field from north-west to south-east (in Galactic coordinates).
- The column density of the more diffuse warm phase is the highest within the contour delimited by the presence of cold gas, but also exists outside of LLIV1.
- The power spectrum of the cold phase is slightly shallower than that of the warm phase, quantifying that the cold phases have relatively more structure on small scales.
- Our spatially resolved map of the cold gas mass fraction in LLIV1 is consistent with the absorption measurement against 4C +66.09 and reveals important variation with  $0.1 \gtrsim f \gtrsim 0.9$ , with mean and standard deviation of 0.33 and 0.19, respectively. Our best model lacks the presence of unstable gas across the whole field of view, similar to the absorption line modeling against 4C +66.09. This possibly suggests that the transition is not on-going and has reached an equilibrium state.

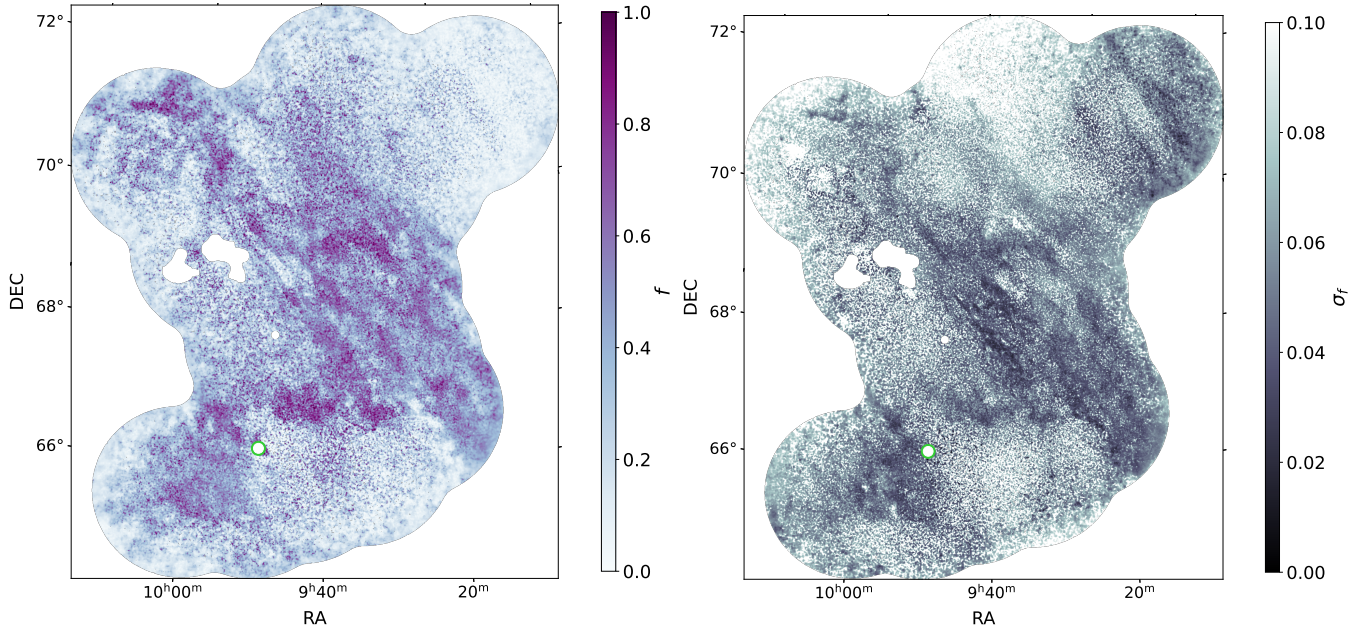


**Figure 11.** CNM mass fraction map inferred from the DHIGLS data.

#### ACKNOWLEDGMENTS

We acknowledge support from the Natural Sciences and Engineering Research Council (NSERC) of Canada. This work took place under the Summer Undergraduate Research Program (SURP) hosted by the University of Toronto. This research has made use of the NASA Astrophysics Data System.

503 Software: Matplotlib (Hunter 2007), NumPy (van der  
504 Walt et al. 2011), and AstroPy<sup>4</sup>, a community-developed  
505 core Python package for Astronomy (Astropy Collaboration  
506 et al. 2013, 2018), SciPy (Virtanen et al. 2020), scikit-image  
507 (van der Walt et al. 2014).

508 APPENDIX

#### 509 A. PARAMETER MAPS OF INDIVIDUAL GAUSSIAN 510 COMPONENTS (GHIGLS)

511 Figure A1 shows the column density maps of each Gaussian sorted by increasing column density-weighted mean velocities (see Table 2). Figures A2 and A3 shows the corresponding velocity fields and dispersion velocity fields. Note, 515 the labels overlaid on the panels in Figure A1 help to associate them with the clusters in Figure 6: e.g., for  $G_2$  (row 2, 516 column 1), “ $G_2$  CNM 2.1” indicates the name of the Gaussian component, the thermal phase, and the column density-weighted mean velocity dispersion  $\langle \sigma_n \rangle$  in  $\text{km s}^{-1}$  as tabulated in Table 2.

#### 521 B. IMPACT OF SPATIAL RESOLUTION ON THE LINE

522 Figure B4 illustrates the impact of spatial resolution on a line of sight within the DHIGLS field of view chosen for its distinct double peaks property. The purple line shows the original DHIGLS data, and the red and blue line show the same data but convolved at 2' and 9'.4, respectively.

#### 527 C. PARAMETER MAPS OF INDIVIDUAL GAUSSIAN 528 COMPONENTS (DHIGLS)

<sup>4</sup> <http://www.astropy.org>

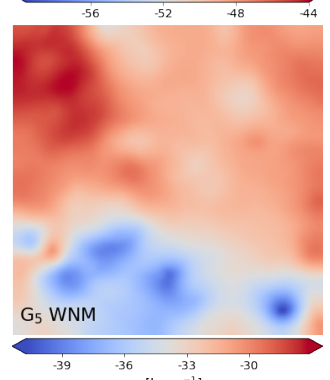
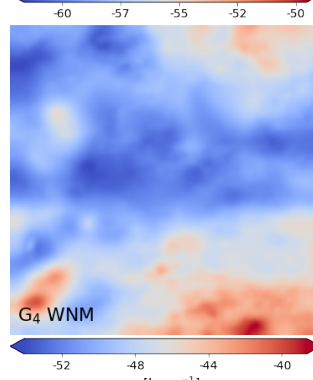
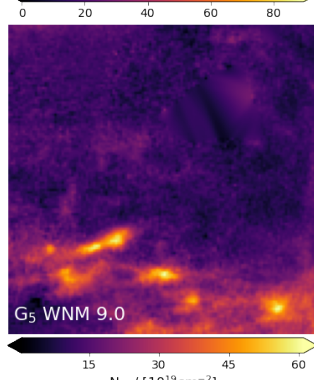
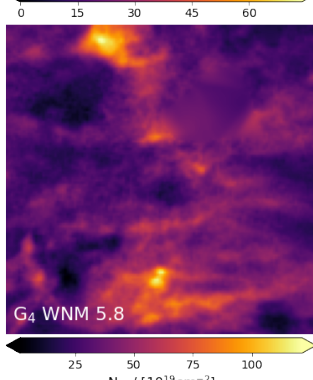
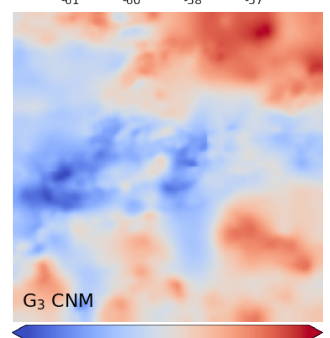
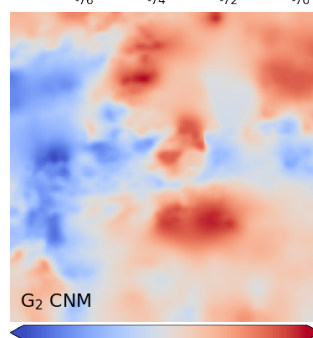
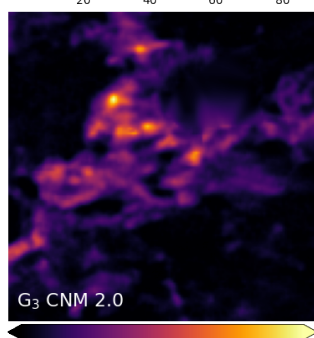
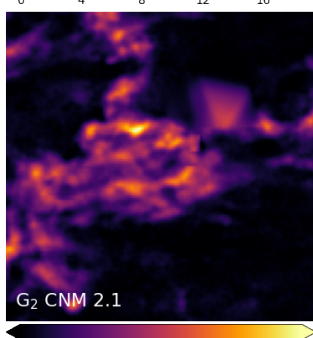
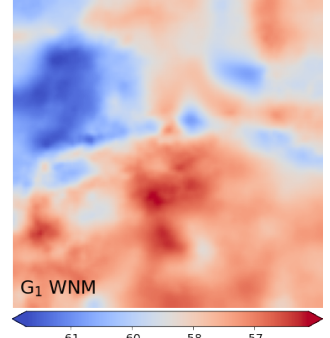
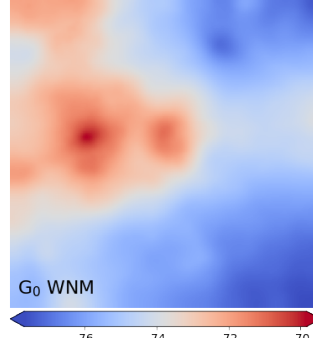
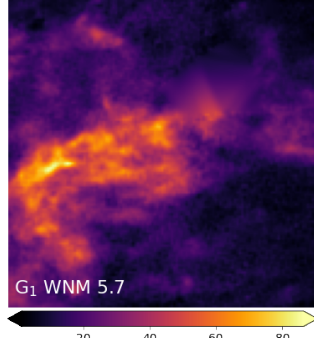
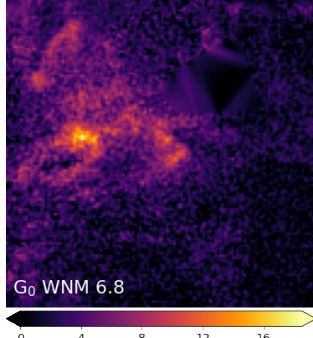


**Figure A1.** Mosaic of  $N_{HI}$  maps of the individual Gaussian components. The maps are sorted by mean velocity. The labels in the bottom left corner represent the sorting of that particular Gaussian component. The number is the mean velocity dispersion ( $\sigma$ ) in units of  $\text{km s}^{-1}$ .

**Figure A2.** Mosaic like Fig. A1, but of maps of the mean velocity  $\mu$  of the Gaussian components.

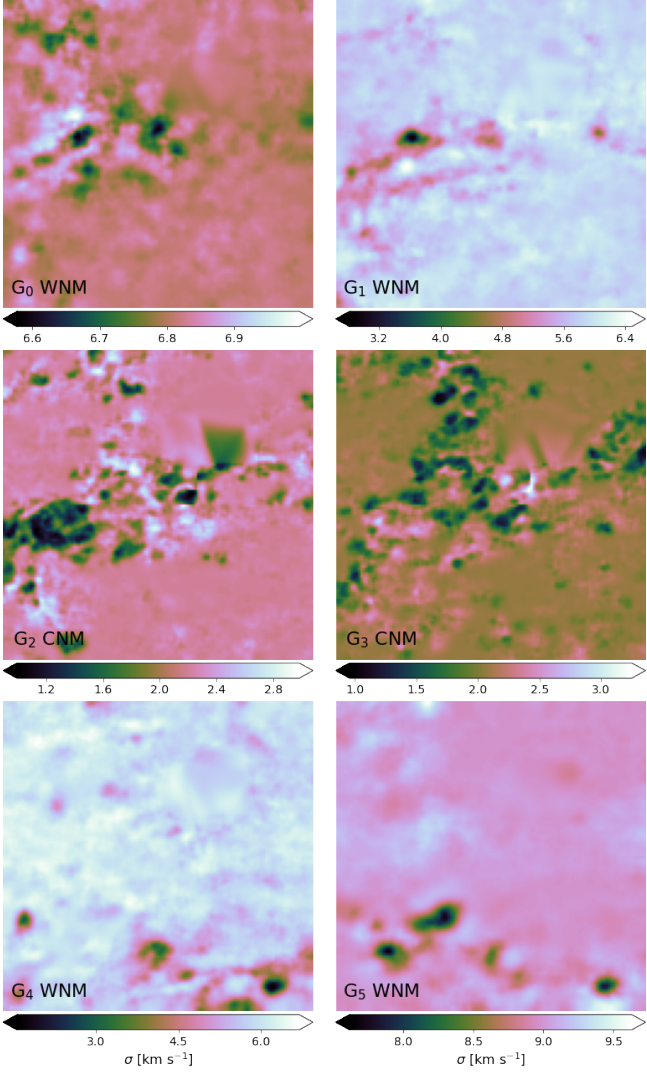


**Figure A3.** Mosaic like Fig. A1, but of maps of the velocity dispersion  $\sigma$  of the Gaussian components.

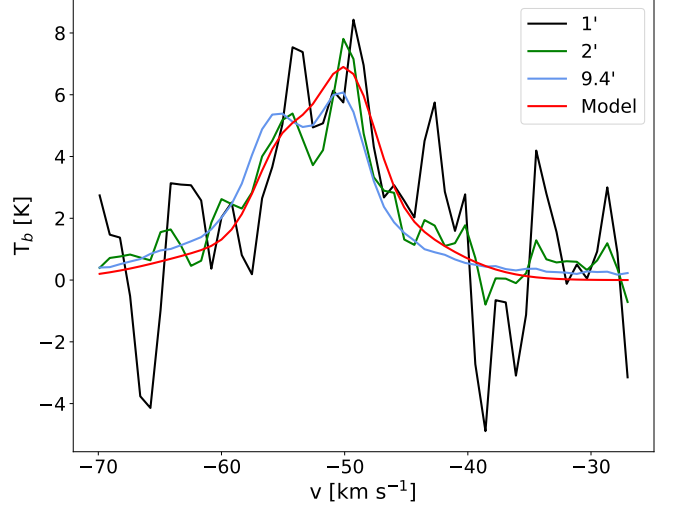


**Figure B4.** Spectrum showing a double peak of cold gas within the DHIGLS field of view. The black line shows the original DHIGLS data, and the green and blue line show the same data but convolved at 2' and 9.4', respectively. The red line shows the model fit to the DHIGLS data at 1'.

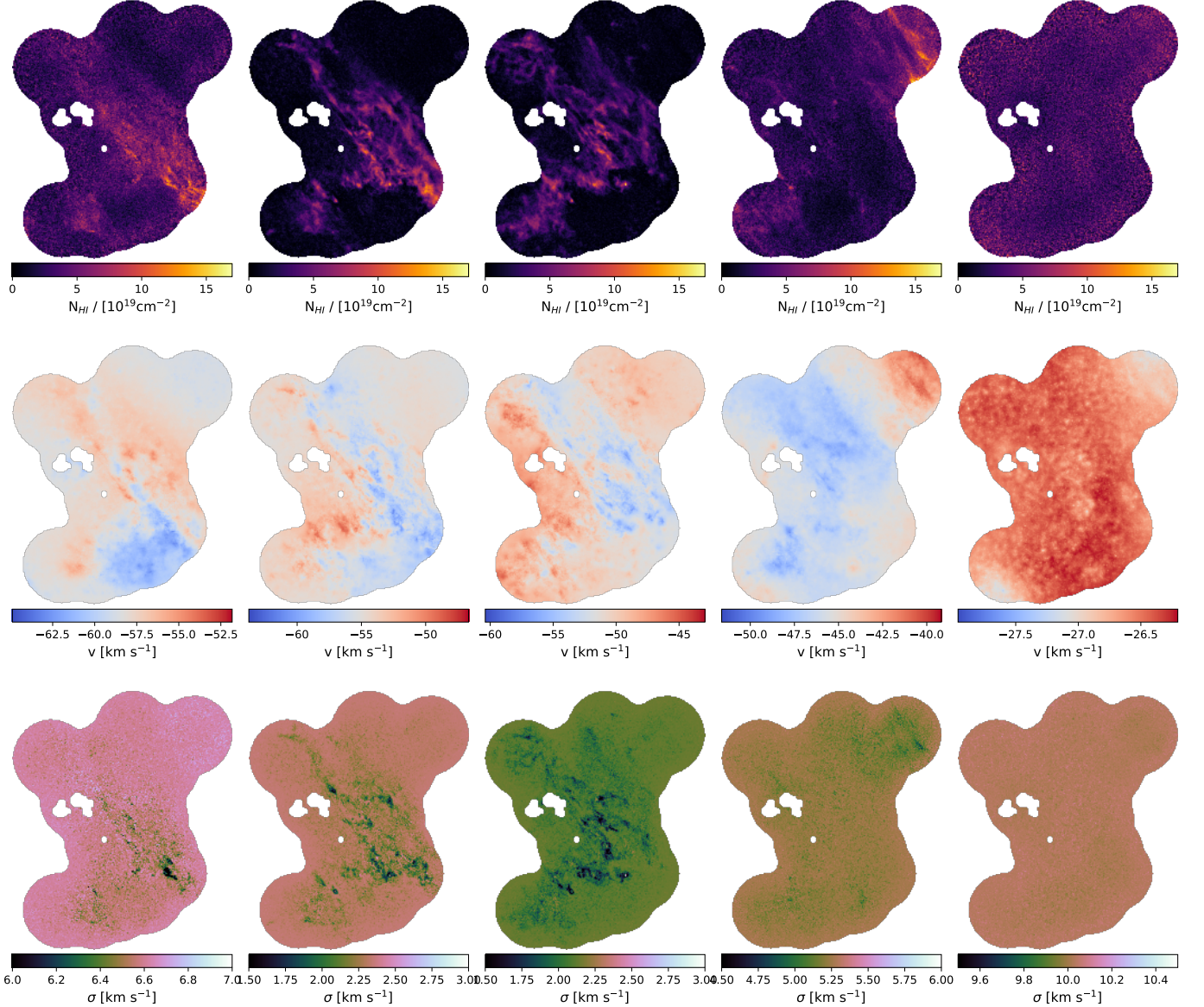


**Figure C5.** Column density maps (top) of Gaussian components identified in the IVC gas (incl. LLIV1) from the DHIGLS data. The middle and bottom rows show the corresponding velocity maps and dispersion velocity maps, respectively.

## REFERENCES

- 529 Astropy Collaboration, Robitaille, T. P., Tollerud, E. J., et al. 2013,  
 530 A&A, 558, A33, doi: [10.1051/0004-6361/201322068](https://doi.org/10.1051/0004-6361/201322068)
- 531 Astropy Collaboration, Price-Whelan, A. M., Sipőcz, B. M., et al.  
 532 2018, AJ, 156, 123, doi: [10.3847/1538-3881/aabc4f](https://doi.org/10.3847/1538-3881/aabc4f)
- 533 Blagrave, K., Martin, P. G., Joncas, G., et al. 2017, ApJ, 834, 126,  
 534 doi: [10.3847/1538-4357/834/2/126](https://doi.org/10.3847/1538-4357/834/2/126)
- 535 Boothroyd, A. I., Blagrave, K., Lockman, F. J., et al. 2011, A&A,  
 536 536, A81, doi: [10.1051/0004-6361/201117656](https://doi.org/10.1051/0004-6361/201117656)
- 537 Bregman, J. N. 1980, ApJ, 236, 577, doi: [10.1086/157776](https://doi.org/10.1086/157776)
- 538 Condon, J. J., Cotton, W. D., Greisen, E. W., et al. 1998, AJ, 115,  
 539 1693, doi: [10.1086/300337](https://doi.org/10.1086/300337)
- 540 de Boer, K. S., Rodriguez Pascual, P., Wamsteker, W., et al. 1993,  
 541 A&A, 280, L15
- 542 Houck, J. C., & Bregman, J. N. 1990, ApJ, 352, 506,  
 543 doi: [10.1086/168554](https://doi.org/10.1086/168554)
- 544 Hunter, J. D. 2007, CSE, 9, 90, doi: [10.1109/MCSE.2007.55](https://doi.org/10.1109/MCSE.2007.55)
- 545 Kuntz, K. D., & Danly, L. 1996, ApJ, 457, 703,  
 546 doi: [10.1086/176765](https://doi.org/10.1086/176765)
- 547 Marchal, A., Martin, P. G., & Gong, M. 2021, ApJ, 921, 11,  
 548 doi: [10.3847/1538-4357/ac0e9d](https://doi.org/10.3847/1538-4357/ac0e9d)
- 549 Marchal, A., & Miville-Deschénes, M.-A. 2021, ApJ, 908, 186,  
 550 doi: [10.3847/1538-4357/abd108](https://doi.org/10.3847/1538-4357/abd108)
- 551 Marchal, A., Miville-Deschénes, M.-A., Orieux, F., et al. 2019,  
 552 A&A, 626, A101, doi: [10.1051/0004-6361/201935335](https://doi.org/10.1051/0004-6361/201935335)
- 553 Martin, P. G., Blagrave, K. P. M., Lockman, F. J., et al. 2015, ApJ,  
 554 809, 153, doi: [10.1088/0004-637X/809/2/153](https://doi.org/10.1088/0004-637X/809/2/153)
- 555 Miville-Deschénes, M. A., Salomé, Q., Martin, P. G., et al. 2017,  
 556 A&A, 599, A109, doi: [10.1051/0004-6361/201628289](https://doi.org/10.1051/0004-6361/201628289)
- 557 Planck Collaboration XXIV. 2011, A&A, 536, A24,  
 558 doi: [10.1051/0004-6361/201116485](https://doi.org/10.1051/0004-6361/201116485)
- 559 Richter, P., Savage, B. D., Wakker, B. P., Sembach, K. R., &  
 560 Kalberla, P. M. W. 2001, ApJ, 549, 281, doi: [10.1086/319070](https://doi.org/10.1086/319070)
- 561 Richter, P., Wakker, B. P., Savage, B. D., & Sembach, K. R. 2003,  
 562 ApJ, 586, 230, doi: [10.1086/346204](https://doi.org/10.1086/346204)
- 563 Shapiro, P. R., & Field, G. B. 1976, ApJ, 205, 762,  
 564 doi: [10.1086/154332](https://doi.org/10.1086/154332)
- 565 Taank, M., Marchal, A., Martin, P. G., & Vujeva, L. 2022, ApJ,  
 566 937, 81, doi: [10.3847/1538-4357/ac8b86](https://doi.org/10.3847/1538-4357/ac8b86)
- 567 van der Walt, S., Colbert, S. C., & Varoquaux, G. 2011, CSE, 13,  
 568 22
- 569 van der Walt, S., Schönberger, J. L., Nunez-Iglesias, J., et al. 2014,  
 570 PeerJ, 2, e453, doi: [10.7717/peerj.453](https://doi.org/10.7717/peerj.453)
- 571 Virtanen, P., Gommers, R., Oliphant, T. E., et al. 2020, Nature  
 572 Methods, 17, 261,  
 573 doi: <https://doi.org/10.1038/s41592-019-0686-2>
- 574 Wakker, B. P. 2001, ApJS, 136, 463, doi: [10.1086/321783](https://doi.org/10.1086/321783)